Macalester Journal of Physics and Astronomy

Volume 12
Issue 1 *Spring 2024*

Article 7

May 2024

Strain methods for changing local electric field gradient in BaFe2As2

Caleb Williams
Macalester College, willcal2020@gmail.com

Strain methods for changing local electric field gradient in BaFe2As2

Abstract

In this study, we introduce a novel approach aimed at advancing the investigation of local nematicity in BaFe2As2 via dynamically pulsed strain fields. Our research is motivated by the pursuit of a more sensitive alternative to existing static strain methods. Employing nuclear magnetic resonance techniques, we measure the nuclear quadrupolar energy splittings, utilizing them as a sensitive indicator of the electric field gradient (EFG) that couples strongly to the orbital occupations of the 75As p-orbitals. In the new method, we discern an EFG response through changes in the phase acquired by the nuclear magnetization while time-evolving in the strain field, as opposed to a change in resonance frequency under constant strain. The previous technique measured a linear response in the EFG to applied strain and extracted the nematic susceptibility from these slopes as a function of temperature. The susceptibility diverged near the known structural transition and agreed with elastoresistance measurements. Our technique replicates the static results but proves three orders of magnitude more sensitive and hence requires less strain, establishing one of the first methods for probing nematic degrees of freedom within the superconducting regime.

Keywords

NMR, resonance, strain

MACALESTER COLLEGE

Strain methods for changing local electric field gradient in $BaFe_2As_2$

by

Caleb Williams

in the

Department of Physics and Astronomy

Advisors: N.J. Curro [1] J. Heyman [2]

April 2024

[1]University of California, Davis
[2]Macalester College

MACALESTER COLLEGE

Abstract

Department of Physics and Astronomy

by Caleb Williams

In this study, we introduce a novel approach aimed at advancing the investigation of local nematicity in $BaFe_2As_2$ via dynamically pulsed strain fields. Our research is motivated by the pursuit of a more sensitive alternative to existing static strain methods. Employing nuclear magnetic resonance techniques, we measure the nuclear quadrupolar energy splittings, utilizing them as a sensitive indicator of the electric field gradient (EFG) that couples strongly to the orbital occupations of the ^{75}As p-orbitals. In the new method, we discern an EFG response through changes in the phase acquired by the nuclear magnetization while time-evolving in the strain field, as opposed to a change in resonance frequency under constant strain. The previous technique measured a linear response in the EFG to applied strain and extracted the nematic susceptibility from these slopes as a function of temperature. The susceptibility diverged near the known structural transition and agreed with elastoresistance measurements. Our technique replicates the static results but proves three orders of magnitude more sensitive and hence requires less strain, establishing one of the first methods for probing nematic degrees of freedom within the superconducting regime.

Acknowledgements

I'd like to express my sincere gratitude to my research advisor Dr. Nicholas Curro for allowing me to participate in this meaningful work. I am also grateful for the guidance of my local advisor Dr. James Heyman while crafting this honors thesis. Finally, additional thanks to my fellow peers in the Macalester Physics and Astronomy department for unwavering support and friendship.

Contents

List of Figures

List of Tables

CHAPTER 1: Introduction

1.1 Motivation

Our experiment is motivated by the desire to better understand what characteristics give rise to superconductivity in metals. The complex interplay between orbital, magnetic, and lattice degrees of freedom within iron-based superconductors has made this question historically difficult to answer. We are particularly interested in investigating 'nematicity', the directional dependence observed when measuring certain nuclear properties, in strongly correlated electron systems (SCES). The response of these properties to external stress is known as nematic susceptibility, visible through changes in the energy splitting of nuclear spin states. Studying this phenomenon could lend insight into the relationship between nematicity and the superconducting mechanism as a whole.

This study outlines the development of a novel technique for probing the nematic susceptibility of atomic nuclei. Employing Nuclear Magnetic Resonance (NMR) techniques, combined with the precise application of time dependent strain fields, allows us to study *local* nematicity and overcome problems previously associated with exploring nematic degrees of freedom in critical regimes. To validate our method, we test it with a non-superconductive crystal, $BaFe_2As_2$, that is well-studied and readily available. By reproducing known nematic susceptibility measurements, we can confirm the effectiveness of our technique before applying it to a superconductor. This experiment has been done previously using static strain, however, pulsed strain is nearly one thousand times more sensitive, hence requiring less strain and permitting the measurement of more fragile materials. Chapter 1 covers the relevant theory, a review of NMR and the predicted behavior for a strained nuclear magnetization.

1.2 Nuclear Magnetic Resonance

This section provides an introduction to Nuclear Magnetic Resonance (NMR) experiments, a type of spectroscopy utilized in many scientific fields. We will discuss how this technique probes nuclear energy transitions and how we can use it in conjunction with compressive or tensile strain. After reviewing the NMR theory, we can explore our unique approach for stress application on crystals.

NMR helps physicists study the magnetic properties of atomic nuclei and understand molecular structures by probing interactions between nuclei (with a non-zero spin magnetic moment) and external magnetic fields. The spin magnetic dipole moment of a nucleus can be expressed as the vector:

$$\vec{\mu_s} = g\frac{e}{2m}\vec{I} = \gamma\vec{I} \tag{1.1}$$

where γ is the gyromagnetic ratio, e is the elementary charge unit, m is the mass of the particle, $\vec{I}$ is the spin and g is a dimensionless number known as the 'g-factor' of the nucleus. The interaction between this magnetic moment and an external field causes spin states to become non-degenerate in energy. As a result, nuclei can transition between spin states by absorbing or emitting specific amounts of energy. The possible energy states for a simple spin $\frac{1}{2}$ system are governed by the Zeeman Hamiltonian below and depicted in Fig 1.1:

$$H = -\gamma\hbar H_0\hat{I} \tag{1.2}$$

$$E = \pm g\frac{e\hbar}{2m}B \tag{1.3}$$

Here, $\hbar$ is Planck's reduced constant, H_0 is the external magnetic field, and the spin operator $\hat{I} = I_z$ in our experiment. It's important to remember that nuclei can be in a superposition of multiple spin states. In the case of a spin $\frac{1}{2}$ nucleus, a single measurement of the energy must return one of the two allowable values. The expectation value, however, is the average of many energy measurements and can

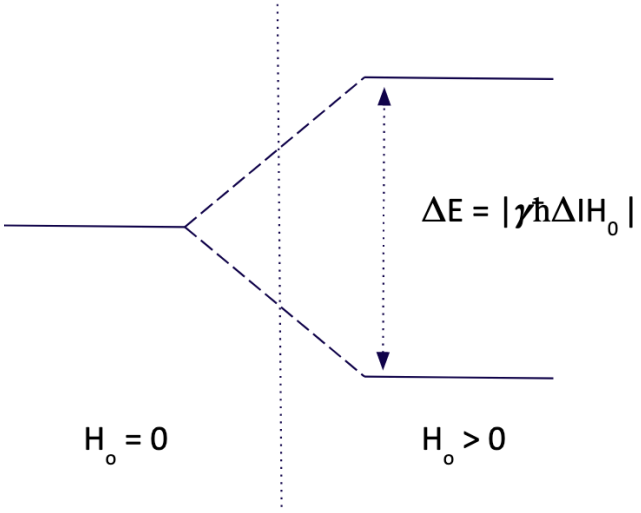

FIGURE 1.1: The energy difference between the spin states of a spin $\frac{1}{2}$ particle governed by the Zeeman Hamiltonian.

tell us about the probability of finding a nucleus in a given state. A Bloch sphere is a classical representation of superposition where the probability is represented by the direction of a state vector. Bloch spheres will be useful for tracking the evolution of a nuclear spin over the course of our NMR experiment. If we again consider a spin $\frac{1}{2}$ particle, then Fig 1.2 depicts just a few possible orientations of a spin state vector.

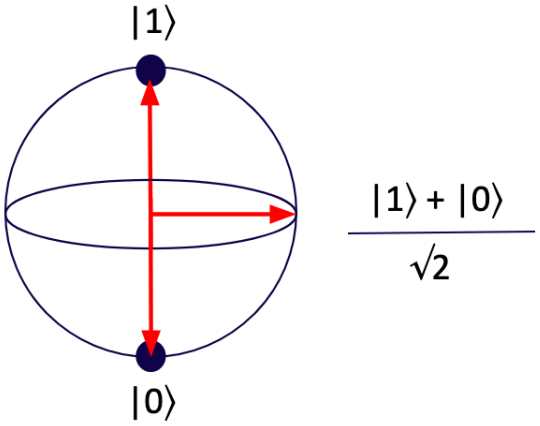

FIGURE 1.2: A few possible orientations of a state vector in a spin $\frac{1}{2}$ Bloch Sphere.

While a spin $\frac{1}{2}$ particle only has two states and one transition, the ^{75}As nuclei in $BaFe_2As_2$ are spin $\frac{3}{2}$. This means that there are four spin states and three possible transitions. In this case the Zeeman Hamiltonian will no longer be accurate. These nuclei have a non-spherical charge distribution and exhibit a quadrupolar moment that couples to the local electric field gradient (EFG), the second derivative of electric potential. As a result, the energy levels of nuclear spin states are no longer equally spaced. Quadrupolar contributions to the Hamiltonian are denoted as $\pm\nu_q$ in Fig 1.3.

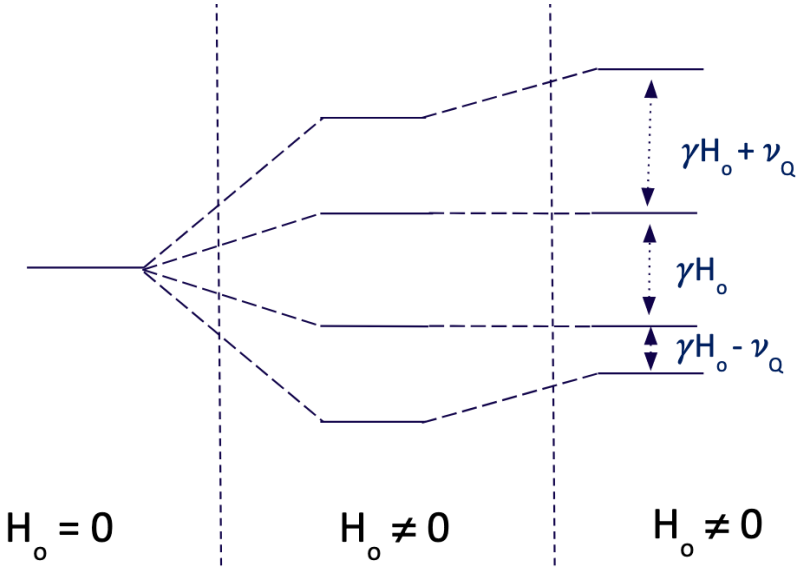

FIGURE 1.3: The energy difference between the spin states of a spin $\frac{3}{2}$ particle after considering the quadrupolar interaction.

For a spin $\frac{3}{2}$ nucleus like ^{75}As, the highest and lowest energy gaps are known as 'satellite' frequencies. NMR experiments excite nuclei to different spin states by applying radiofrequency (RF) pulses at the precise energies corresponding to these transitions. By observing how spins react to a pulse, we can make assumptions about the atomic structure of a compound. The next section describes how RF pulses are used to measure resonance frequencies.

1.2.1 RF Excitation

Typical NMR experiments begin by placing a crystal in a strong external magnetic field, causing a net magnetization of the nuclear spins to point in the same direction (say the z-axis). This is the lowest energy state of the prepared system. A RF pulse is applied to the sample with an energy matching a specific transition of ^{75}As. The energy from this RF pulse can be absorbed by the nuclei, and when applied for the correct amount of time, it orchestrates a rotation of the nuclear spins (and thus the net magnetization) away from the z-axis and into the xy plane. A $\frac{\pi}{2}$ pulse is one that rotates the net magnetization by 90 degrees. Once in plane, the spins precess at the Larmor frequency, the same frequency as the $\frac{\pi}{2}$ pulse. We can detect the electromagnetic radiation produced by these spins and apply a Fourier Transform to deduce the contributing resonance frequencies.

There are three main contributions to the loss of signal in the xy plane. T_1 is known as the energy relaxation time - the time constant for spins to lose their excitation energy and return to thermal equilibrium, parallel to the z-axis. A second time constant, T_2, considers the decrease of net magnetization due the loss of coherence among precessing spins. This decoherence is known as 'spin-dephasing' and arises due to spin-spin and spin-lattice interactions. T_2 strictly involves the dephasing caused by important microscopic processes. T_2^* is the combination of T_2 and additional contributions by inhomogeneities in the magnetic field or crystal lattice. The important idea is that in-plane spin precession, and therefore magnetization signal, will not be measurable forever. Fig 1.4 depicts this process from a spin's frame of reference.

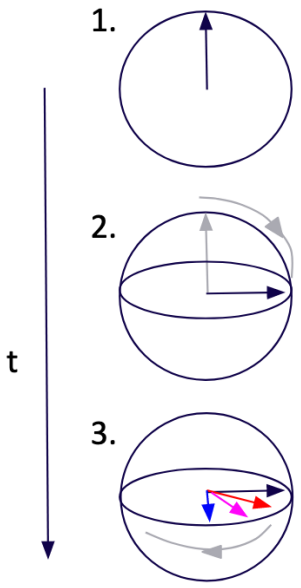

FIGURE 1.4: Time evolution of nuclear spin response to RF pulse. Step 1. Spins are polarized in the z-direction. Step 2. Coherent rotation into the xy plane. Step 3. Dephasing during spin precession in xy plane, shown in rotating frame of reference.

It turns out that T_2^* related effects destroy the signal much faster than any other process. Hahn Echo NMR is a technique that uses multiple RF pulses to mitigate this inhomogenious dephasing during spin precession, isolating T_2 effects. The next section introduces this pulse sequence before discussing it's importance in the context of strain.

1.2.2 Hahn Echo NMR

Hahn Echo NMR begins with the same setup described in the previous section. An external magnetic fields causes a net magnetization of nuclear spins to point in the z direction. We then apply a $\frac{\pi}{2}$ RF pulse to rotate the spins into the xy plane where they precess at the Larmor frequency. A wait time τ is introduced, and the nuclear spins begin to dephase. To counteract this dephasing, we apply a second, 'π', RF pulse at time τ with the same frequency as the $\frac{\pi}{2}$ pulse. A π pulse is twice as long as a $\frac{\pi}{2}$ pulse, rotating the nuclear spins an additional 180 degrees while also inverting their phase. This inversion of phase causes the spins that were

previously furthest ahead to now be furthest behind (see Fig 1.5). The previously dephasing spins to refocus and form an echo signal, which occurs at time 2τ. A schematic diagram for a Hahn Echo sequence is depicted in Fig 1.6.

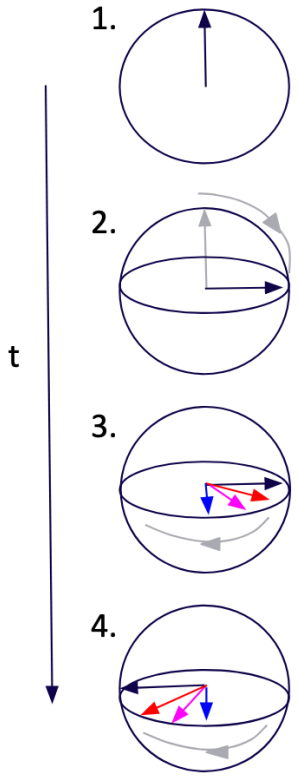

FIGURE 1.5: Time evolution of nuclear spins in an echo pulse sequence. Step 1. Spins are polarized in the z-direction. Step 2. Coherent rotation into the xy plane. Step 3. Dephasing during spin precession in xy plane, shown in rotating frame of reference. Step 4. The phase of each of the spins is inverted and they begin to refocus.

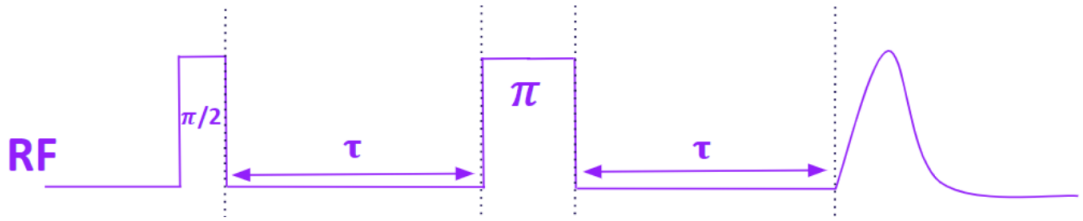

FIGURE 1.6: The Hahn Echo pulse sequence. Diagrams two radio frequency pulses used to knock the spins by $\frac{\pi}{2}$ and then π radians. An echo appears at exactly the time t = 2τ.

Applying a Fourier Transform to an echo signal will expose the resonance frequencies of excited nuclei. While a simplified scenario envisions a spectrum that prominently spikes at the Larmor frequency, reality introduces a spectrum with a width governed by dipole broadening and other decoherence effects. We utilize quadrature detection that splits the echo into real and imaginary parts, causing the resulting spectra to contain phase information about the signal. We claim that a small shift in frequency can show up in a phase shift of the echo relative to the RF excitation pulses, visible through the ratio of real to imaginary signal, and that it is a more sensitive alternative to observing a shift in the spectrum itself. Phase is related to a change in frequency by:

$$\Delta\theta = \Delta f \times 2\tau \times 2\pi \tag{1.4}$$

and measurable through:

$$\tan\theta = \frac{\text{IM[signal]}}{\text{RE[signal]]}} \tag{1.5}$$

This idea is the cornerstone of our project. Previous experiments have only used static strain to measure changes in nuclear resonance frequencies directly. Our technique has the ability to measure changes in phase, rather than frequency, by

applying pulsed strain. The next section discusses the difference between these types of strain and how they effect energy transitions.

1.2.3 Strain in NMR

When strain fields act upon a crystal, they exert stress that causes the positions of ions to shift and frequently disrupts lattice symmetries. Consequently, the electric field gradient (EFG) at the nuclei sites becomes asymmetric. Nuclei couple to the EFG through their quadrupolar moment, and because the quadrupolar moment of nuclei has a large effect on the energy splittings of spin states, a change in transition frequency is a sensitive indicator of the EFG's response to strain. In fact, when we say nematic susceptibility, we technically mean the EFG's response to strain, which is proportional to a change in resonance. Nematic susceptibility is also temperature dependent, as conduction electrons and other particles become more or less energized depending on the external environment. The effect of strain is interesting because it probes the nematic degrees of freedom of a material and can be extended below critical temperatures. This could allow a somewhat quantitative analysis regarding the superconducting behavior of metals in their critical regime.

Only recently has a method using what we call 'static' strain been developed to measure nematic susceptibility. Static strain experiments are straightforward, a constant strain is placed on a crystal over the course of many measurements to find the change in resonance frequencies directly. This is done by taking the discrete Fourier transform of the echo, just as in the original NMR experiments, and comparing the strained and unstrained spectra. However, there is an inherent sensitivity constraint for this technique. In order to accurately deduce a change in frequency, we would need the new spectrum to shift by at least half of the width of the original. As mentioned earlier, the width of our Fourier spectra are governed by T_2^* and other decoherence phenomenon. The minimum strain required to produce a noticeable change is:

$$\Delta f = (\frac{df}{d\epsilon_s})\epsilon_s \gtrsim \frac{1}{T_2^*} \tag{1.6}$$

$$\epsilon_s \geq (\frac{df}{d\epsilon_s})^{-1}\frac{1}{T_2^*} \tag{1.7}$$

Where ϵ_s is the magnitude of static strain, $(\frac{df}{d\epsilon_s})$ is the slope of the crystal's response to strain, and T_2^* is the decay constant due to decoherence effects. We notice immediately that crystals with a small T_2^* time will require large amounts of strain to achieve meaningful results.

We look to introduce a pulsed strain sequence, in the form of a square wave alternating between positive and negative strain of the same magnitude. This technique will change the phase acquired by the nuclear magnetization while time-evolving in the strain field, rather than producing a measurable shift in the resonance frequency. A strain pulse changes the resonance frequency of a transition, but once taken away, the spins return to their natural precession frequency. However, the spins are at different points in their precession then they would have been in a completely un-strained case. This difference is what we are referring to as the phase shift. The timing of a strain pulse sequence and its effect on the phase of an echo signal is shown in Fig 1.7.

Switching the order of the positive and negative pulses will also change the outcome. We measure this phase shift and calculate the corresponding change in resonance frequency due to that magnitude of strain. The phase accumulated from a pulse sequence is given by:

$$\delta\theta = 2t_{pulse}(\frac{df}{d\epsilon_p})\epsilon_p \tag{1.8}$$

where t_{pulse} is the same length of time as an ϵ_+ or ϵ_- application. Thus the minimum strain needed to deduce a resonance shift would be:

$$\epsilon_p \gtrsim \delta\theta(2t_{pulse}(\frac{df}{d\epsilon_p}))^{-1} \tag{1.9}$$

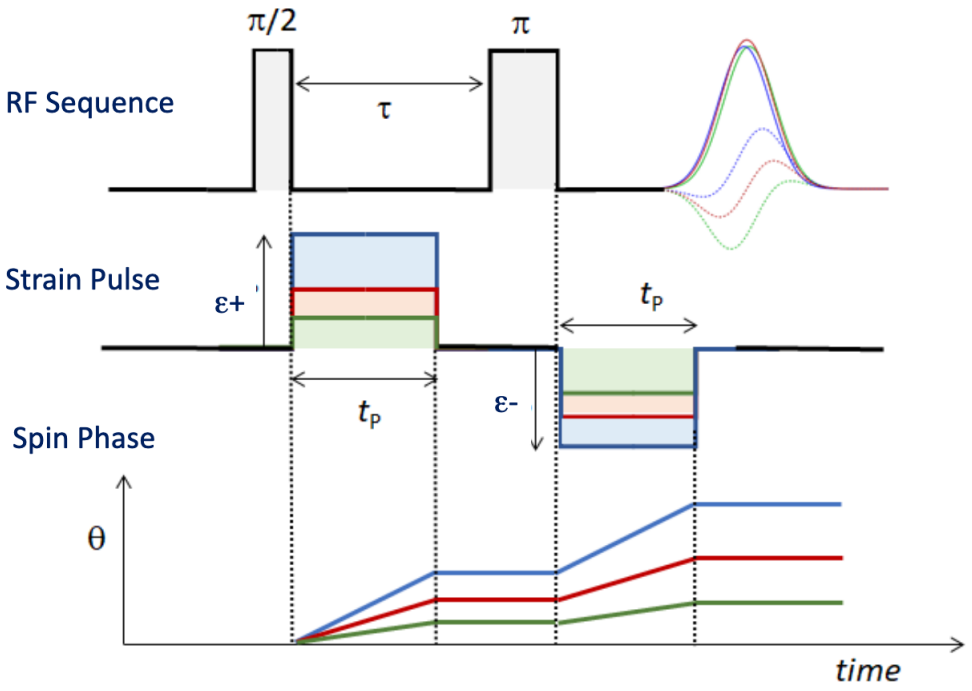

FIGURE 1.7: Strain pulses are applied during free precession. The change in phase in the rotating frame will be proportional to the strain pulse width, t_p, times the strain pulse magnitude, ϵ.

where $\delta\theta$ is now the experimental uncertainty that comes with measuring the phase. The new technique no longer explicitly depends on T_2^*, avoiding most of the problems associated with decoherence effects all together. Let's take a moment to compare the sensitivity of the two methods. If we compare the two sensitivity equations (1.7 and 1.9), we notice that the minimum strain depends on inverse of the slope, $(\frac{df}{d\epsilon})^{-1}$, in both cases. The only relevant information is the T_2^* time for a specific crystal, the uncertainty in our phase measurement, and strain pulse length. In the case of $BaFe_2As_2$, $\frac{1}{T_{2*}}$ has been measured to be approximately 300 kHz $\sim \frac{1}{3}\mu$s (Kitagawa et al. (2008)). For reasons we will explain later, t_{pulse} is optimized in our crystal at 900μs. Thus the static strain minimum becomes:

$$\epsilon_{min} \gtrsim (\frac{df}{d\epsilon_s})^{-1}(T_2^*)^{-1} \sim (\frac{df}{d\epsilon_s})^{-1}(3.3 * 10^6) \tag{1.10}$$

While the pulsed strain minimum is:

$$\epsilon_{min} \gtrsim \frac{5(df/d\epsilon_p)^{-1}}{2t_{pulse}} \sim (\frac{df}{d\epsilon_s})^{-1}(2.7 * 10^3) \tag{1.11}$$

Therefore we predict that phase detection could be as many as three orders of magnitude more sensitive, hence requiring less strain.

As mentioned before, we can apply a Fourier Transform to the real and imaginary echo and analyze the resulting spectra. If we repeat the experiment for a few different magnitudes of pulsed strain, we would expect to observe a change in the the ratio of real to imaginary signal intensity. Fig. 7 is a conceptual drawing of how the signal ratio may change with different values of strain.

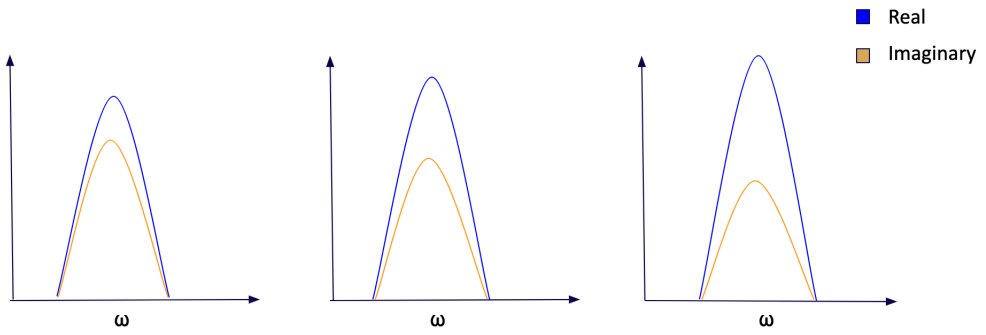

FIGURE 1.8: Conceptual depiction of the phase in the real and imaginary spectra as we sweep strain. The horizontal axis corresponds to the spin's precession frequency while the vertical axis is in arbitrary units of intensity.

In this chapter, we established NMR spectroscopy as a method for measuring the energy difference between nuclear spin states. The Hahn Echo pulse sequence is useful for limiting the effects of crystal inhomogeneities on signal intensities, something that becomes a problem in the critical regime of metals. Pairing NMR with strain fields provides a way to probe the local nematic susceptibility of a crystal. Although a previous method has been explored using static strain, the idea of phase accumulation from a time-dependent strain field is new and has not been tested before. Therefore, it is important to confirm that our suspicions are correct before trying to design an experiment. Chapter 2 outlines a set of

numerical simulations that used pulsed strain to measure changes in transition frequencies.

CHAPTER 2: QuTIP Simulations

This chapter outlines the development of simulated NMR experiments, designed to test the behavior of nuclear magnetization under the influence of strain. Chapter 1 showed that we expect spins to accumulate phase when precessing in the x-y plane under strain. We elect to use QuTIP, a quantum toolbox in Python, to simulate the time evolution of our quantum system (Johansson et al. (2012)). The system is modelled as a time-dependent Hamiltonian and the software numerically solves the Schrodinger equation at a list of times specified by the user. The Hamiltonian is constructed using spin operators, so this sections revisits a key result from the algebraic theory of spin in quantum mechanics.

Spin is quantized, meaning every elementary particle possesses an inherent and unchangeable spin value. For instance, a particle would be described as having spin $\frac{1}{2}$ if a measurement of the spin in any direction could yield any value from the set $\{-\frac{1}{2}\hbar, \frac{1}{2}\hbar\}$. This quantization condition gives rise to spin operators that represent the projection of spin onto each coordinate axis. Here we give them as 2-dimensional matrices.

$$S^2 = \frac{3}{4}\hbar^2 \begin{pmatrix} 1 & 0 \\ 0 & 1 \end{pmatrix}$$

$$S_x = \frac{\hbar}{2} \begin{pmatrix} 0 & 1 \\ 1 & 0 \end{pmatrix}$$

$$S_y = \frac{\hbar}{2} \begin{pmatrix} 0 & -i \\ i & 0 \end{pmatrix}$$

$$S_z = \frac{\hbar}{2} \begin{pmatrix} 1 & 0 \\ 0 & -1 \end{pmatrix}$$

These matrix forms can be extrapolated to higher dimensions for particles with higher spin values. In this simulation the Hamiltonian describes ^{75}As, the nucleus

we probe in the actual experiment. Despite this, the simulation is quite general and can be modified slightly to fit a number of different scenarios. In $BaFe_2As_2$, strain breaks the original tetragonal symmetry of the lattice, resulting in a new orthorhombic structure and an asymmetric EFG at nuclei sites. We define an asymmetry parameter, η, to be:

$$\eta = \frac{V_{aa} - V_{bb}}{V_{aa} + V_{bb}} \tag{2.1}$$

where V_{aa} and V_{bb} refer to the EFG in the [100] (a) and [010] (b) crystal directions in the orthorhombic phase (Kissikov et al. (2018)). η is proportional to the changes in resonance we will measure in an actual experiment. With this convention, we can move on to define our Hamiltonian operator. It will be easiest to separate the Hamiltonian into time-dependent and time-independent parts, where the time-independent term is not affected by strain and is given as the Zeeman Hamiltonian for a spin $\frac{3}{2}$ particle.

$$H_I = -\gamma\hbar H_0 \hat{I}_z = \omega_0 \hat{I}_z \tag{2.2}$$

Here γ is the gyromagnetic ratio (usually in units of $\frac{MHz}{T}$), $\hbar$ is the reduced Planck's constant, H_0 is the external magnetic field, and $\hat{I}_z$ is the spin z operator. The quadrupolar term, which couples to our strain pulse (and is therefore time-dependent), is slightly more complicated and includes η. For the sake of the simulation, the RF and strain pulses are not applied at the same time. The quadrupolar Hamiltonian contributions are:

$$H_x = V_{zz}\frac{\eta - 1}{2}(3\hat{I_x}^2 - \hat{I}^2) \tag{2.3}$$

$$H_y = V_{zz}(3\hat{I_y}^2 - \hat{I}^2) \tag{2.4}$$

$$H_z = -V_{zz}\frac{(\eta + 1)}{2}(3\hat{I_z}^2 - \hat{I}^2) \tag{2.5}$$

where $\hat{I}_y$ is the spin y operator, $\hat{I}_x$ is the spin x operator, and $\hat{I}^2 = I(I+1)$ multiplied by the identity matrix. The Hamiltonian is split into parts based on spin operator for visualization purposes. Finally, we must model the RF pulse as a change to this time-dependent component. To do this we simply design a series of coefficients that will accompany a second $\hat{I}_x$ contribution, as the RF pulses are applied in the x direction for the simulated experiment.

It is not immediately obvious how long the RF pulse needs to be applied in order for the spins to rotate by 90 and then 180 degrees. For these reasons we ran a series of simulations that acted as a 'nutation' experiment to find the time a $\frac{\pi}{2}$ pulse should be applied. A $\frac{\pi}{2}$ pulse should drive the spin z expectation value into an equal superposition of the two states making up a given transition. Fortunately, QuTIP has the ability to track the expectation values of the spin projections onto each axis. The nutation is done before we apply strain to the system, thus η is set equal to zero. For example, if we consider the central transition (between $\pm\frac{1}{2}$ spin states) in ^{75}As, then a successful t_{90} and t_{180} pulse would cause the spin expectation values to look like they do in Fig 2.1.

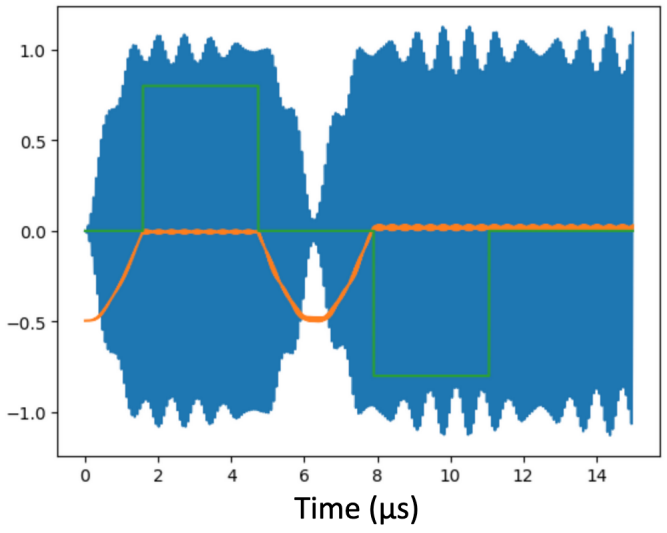

FIGURE 2.1: Spin z (orange) and spin x (blue) expectation values as a function of time with a horizontal axis in units of microseconds. The spin x oscillation is to fast to for resolution on this time scale. The green line depicts the position of a strain pulse sequence.

The same figure also illustrates the inversion of in-plane precessing spins upon the application of the second RF pulse. Keep in mind that t_{180} pulse is applied for exactly twice as long as the t_{90} pulse and is generally of slightly different phase. The figure includes a fake strain pulse sequence (green) to show the timing relationship between RF application and strain. Fig 2.2 focuses on the same simulation, but zooms in on the time interval from 10.5 to 11.5 μs to better show the in-plane spin precessions.

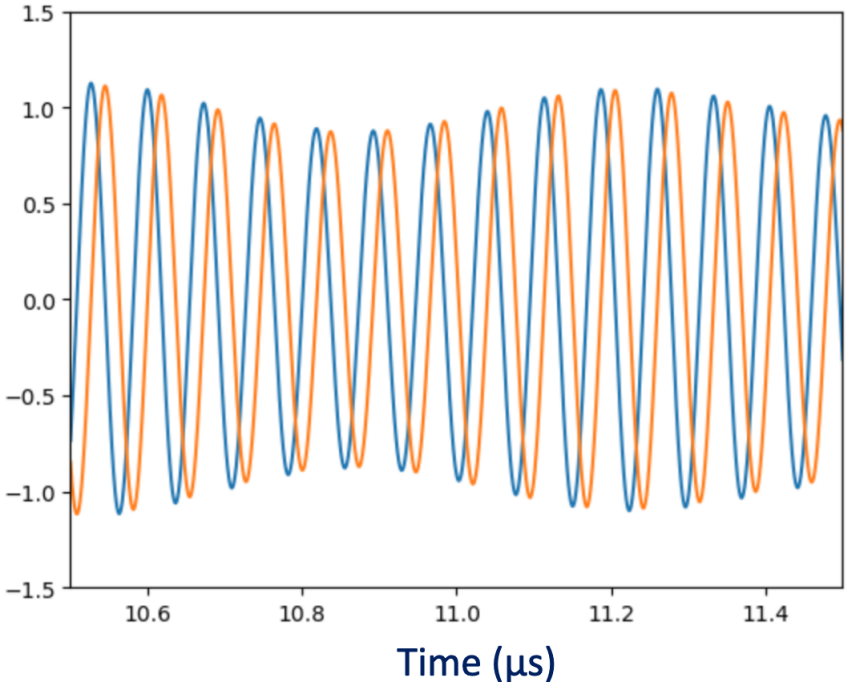

FIGURE 2.2: Fig 2.1 zoomed in on the interval from 10.5 to 11.5 μs, highlighting the evolution of spin x (blue) and spin y (orange) expectation values.

The same nutation process must be performed for each of the satellite transitions as well. Fig 2.3 tracks the spin expectation values while probing the largest energy transition.

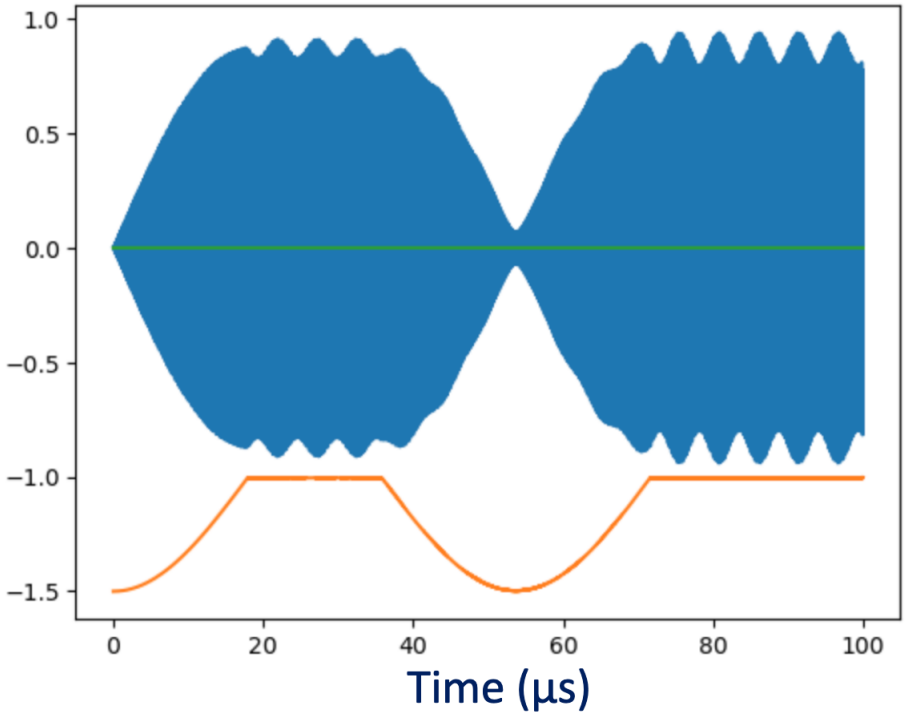

FIGURE 2.3: Spin z (orange) and spin x (blue) expectation values as a function of time for the upper satellite transition. The horizontal axis is in units of microseconds.

The spin x and spin y recession can be represented by a complex signal. When subjected to a Fourier transform, the spin x and spin y signals produce separate 'real' and 'imaginary' spectra whose magnitudes are related by the phase of the complex signal. To measure the effect of strain pulses, we ran a series of simulations where $\eta \in (-0.004, -0.003, -0.002, -0.001, 0, 0.001, 0.002, 0.003, 0.004)$ and observe how the ratio of real to imaginary signal changes with different strains. A subset of the spectra for the upper satellite transition are shown in Fig 2.4. A strain of $\eta = 0.003$ corresponds to a compression of the crystal by 0.3%.

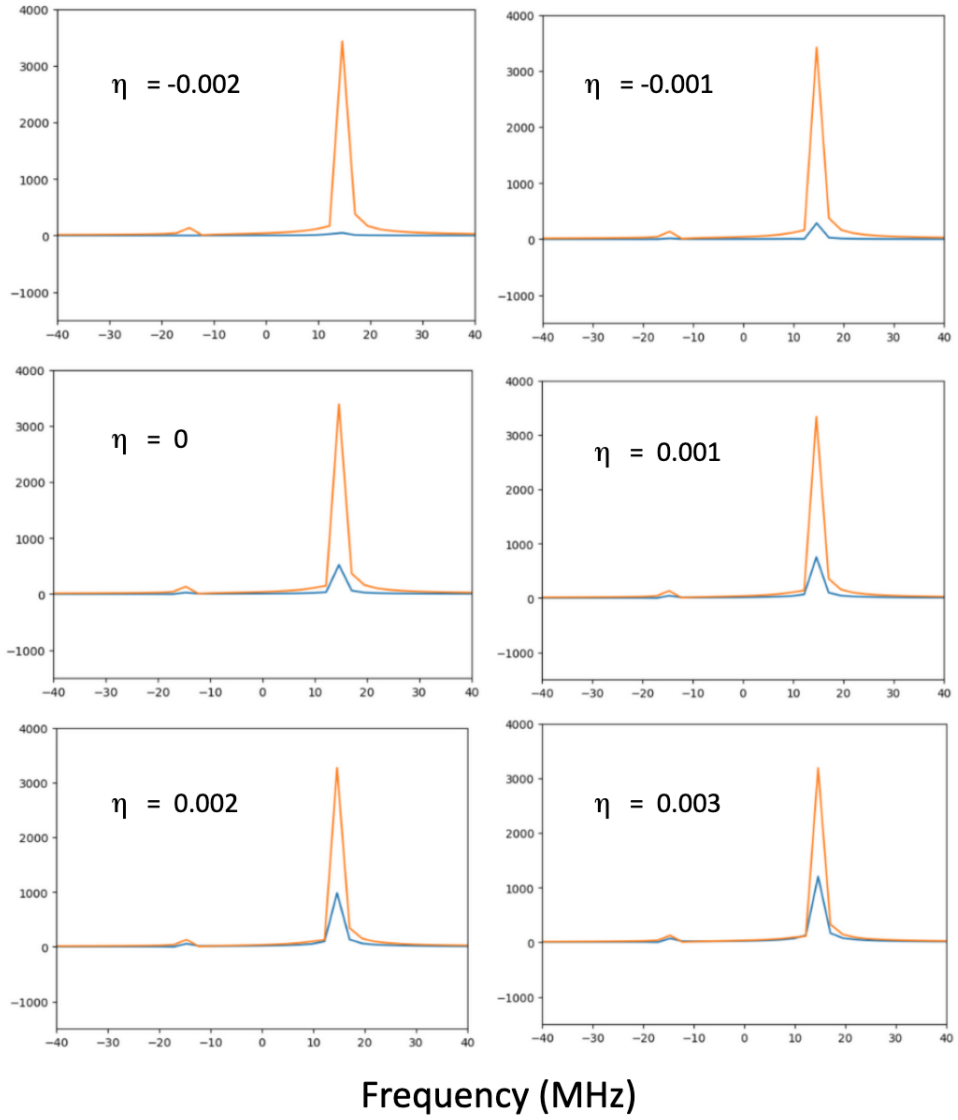

FIGURE 2.4: Real (blue) and Imaginary (orange) spectra for given values of η while probing the upper satellite transition of ^{75}As. The horizontal axis measures frequency in MHz while the vertical axis measures signal intensity.

Indeed, we observe a distinct phase shift between the real and imaginary spectra, even though we have not applied sufficient strain to induce a measurable shift in the resonance frequency. This phase shift, denoted as θ, is related to the frequency shift Δf through the relationship $\theta = 2(\Delta f)\tau$. Upon integrating the spectra, we obtain *scaled* real and imaginary signals, from which we derive a corresponding phase shift, $\theta = \arctan[\frac{\text{Im}}{\text{Re}}]$. Fig 2.5 is an alternative way to plot the intensity of real vs imaginary signal at the specified resonance frequency. This graph shows

that as we increase the magnitude of the strain pulse, the graph 'peaks' at a different ratio of real to imaginary signal.

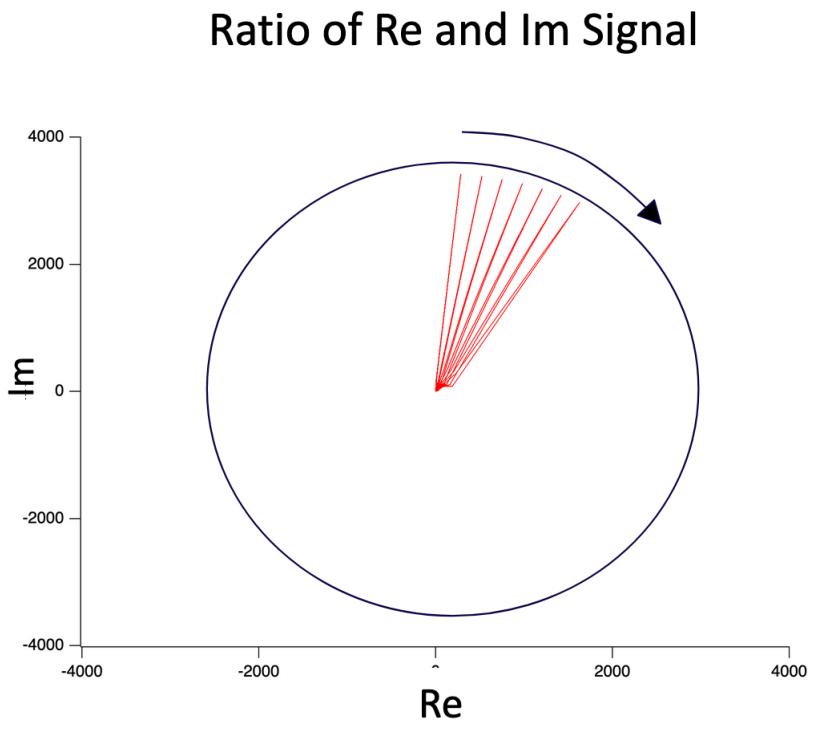

FIGURE 2.5: A plot of the simulated real and imaginary signal intensities as we apply different magnitudes of pulsed strain. Here, frequency is an implicit parameter as peaks only occur at resonance.

Given our anticipation that the scaled signal would exhibit sinusoidal behavior as we sweep strain, the conversion to phase is really just an application of the arctan function. Upon another conversion to degrees, we proceed to divide the result by the duration of the strain pulses to calculate the associated frequency. Table 2.1 examines the shift in upper satellite frequency as a function of η, simulated with parameters that correspond to ^{75}As. The results are then plotted in Fig 2.6. Notice, despite the fact that resonance frequencies of ^{7}5As are on the order of 100 MHz, the pulsed strain technique is measuring frequency shifts on the order of 0.1 KHz. This result confirms the hypothesis that the new method should have a large increase in sensitivity.

η	Scaled	Deg	Adj	Freq (kHz)
-0.002	0.949	71.546	-3.164	-0.122
-0.001	0.957	73.171	-1.538	-0.059
0	0.965	74.709	0	0
0.001	0.971	76.151	1.441	0.056
0.002	0.975	77.233	2.524	0.097

TABLE 2.1: Scaled signal and the calculated frequency shift (kHz) due to simulated strain (η).

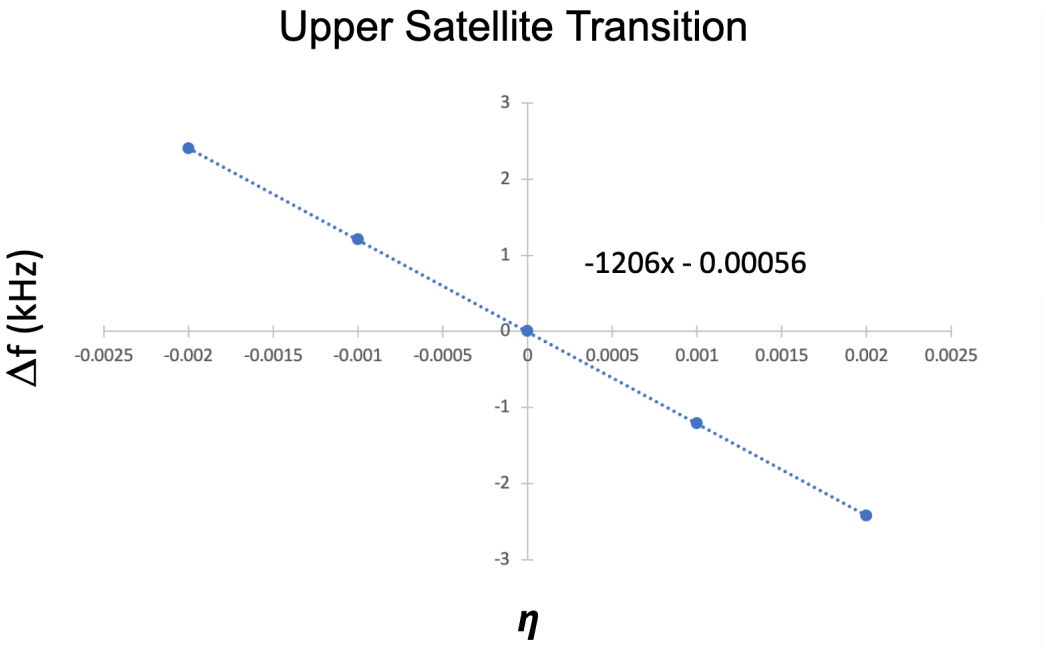

FIGURE 2.6: Frequency shift vs applied strain for the upper satellite frequency in ^{75}As.

The slope of frequency shift vs η matches the predictions for ^{75}As made by perturbation theory. Notice the 'adjusted' frequency column. We can set the zero strain case to be frequency zero because we are only concerned with the *changes* in phase as we sweep strain. Unlike satellite frequencies, the central transition has a second order coupling with the quadrupolar moment, but behaves linearly when η is close to zero. Table 2.2, Figure 2.7 and Figure 2.8 explore the central transition as a function of eta.

η	Scaled	Deg	Adj	Freq (kHz)
0.03	0.9798	78.462	0.845	0.470
0.02	0.9787	78.144	0.527	0.293
0.01	0.9776	77.858	0.241	0.134
0	0.9767	77.617	0	0
-0.01	0.9760	77.428	-0.189	-0.105
-0.02	0.9755	77.298	-0.319	-0.177
-0.03	0.9753	77.231	-0.386	-0.214

TABLE 2.2: Scaled signal and the calculated frequency shift of the central transition in ^{75}As (kHz) due to simulated strain (η).

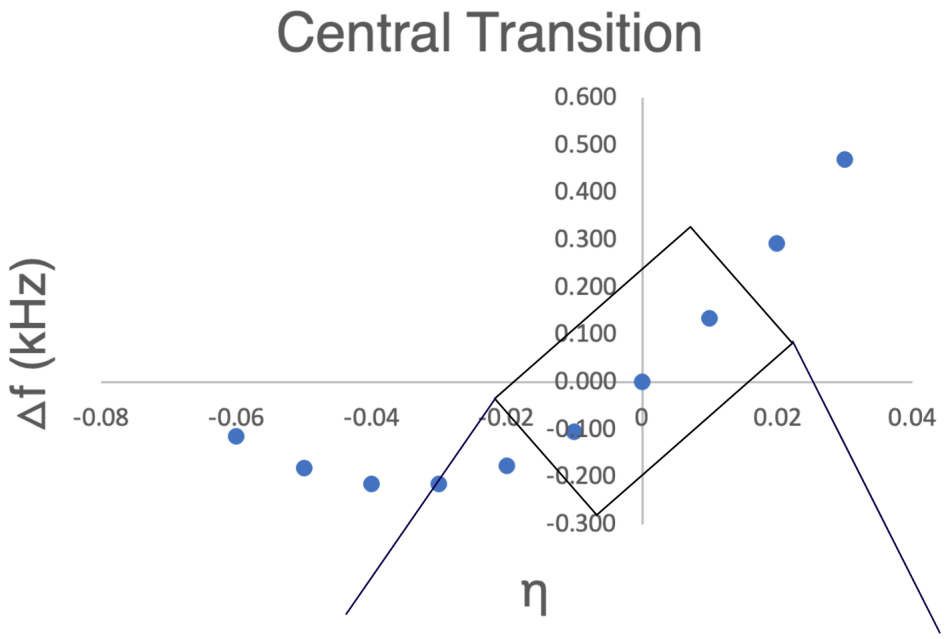

FIGURE 2.7: Frequency shift vs applied strain for the central transition in ^{75}As.

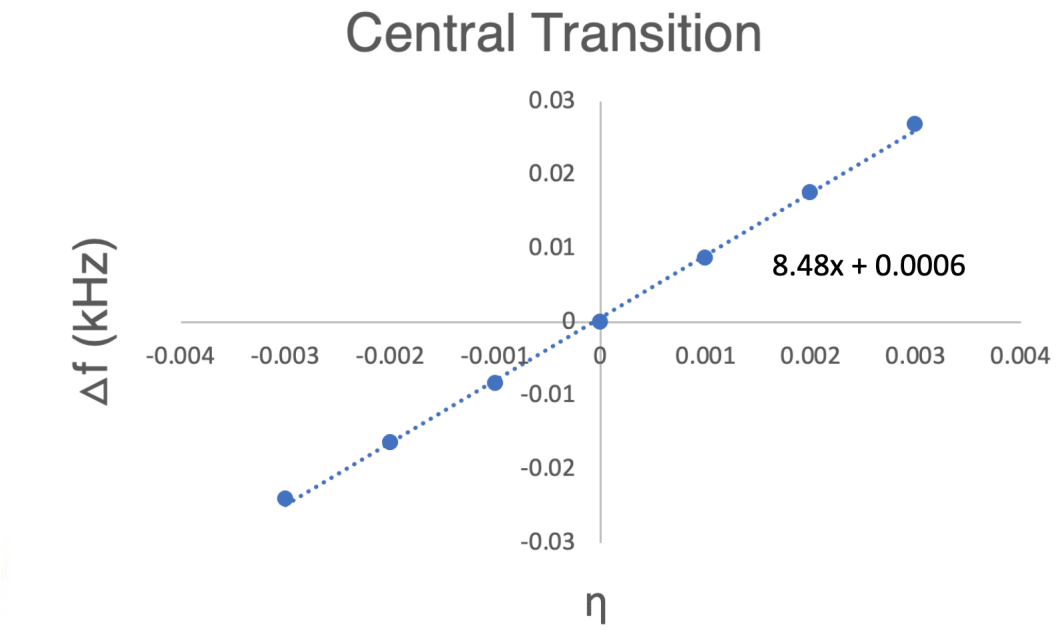

FIGURE 2.8: Zoomed in look at the frequency shift vs applied strain around $\eta = 0$ for the central transition in ^{75}As.

Again this slope seems to agree with perturbation theory, which would predict a slope of approximately 8 kHz per unit η, highlighting its relevance to experimental settings.

This chapter explored the use of Qutip to simulate strained NMR experiments. We modelled the system as a time-dependent Hamiltonian using the common spin operators and tracked the expectation values of S_x, S_y and S_z throughout our potential experiment. Not only did we observe the predicted phase accumulation discussed in Chapter 1, but the results had a quantitative agreement with perturbation theory. These results support an effort to observe the same results in a lab setting. Chapter 3 outlines our implementation of this experiment.

CHAPTER 3: Experiment

3.1 $BaFe_2As_2$

The goal of this experiment is to measure the nematic susceptibility of $BaFe_2As_2$, a parent compound for a family of Iron-Arsenide superconductors. While not in itself superconductive, $BaFe_2As_2$ is very complex and matches the physical and electric characteristics desired by a test crystal. The compound is not overly fragile and has a large signal, making it ideal for the development of our technique. In the absence of a strain field, $BaFe_2As_2$ undergoes a weak first order antiferromagnetic phase transition and a lattice distortion at around 135K. The original tetragonal symmetry of the crystal is broken, producing an orthorhombic structure, lifting the degeneracy of certain Fe d-orbitals, a phenomenon closely related to the development of antiferromagnetism Curro et al. (2022). The ordered regime is preceded by a divergence of nematic susceptibility as temperature approaches the natural phase transition.

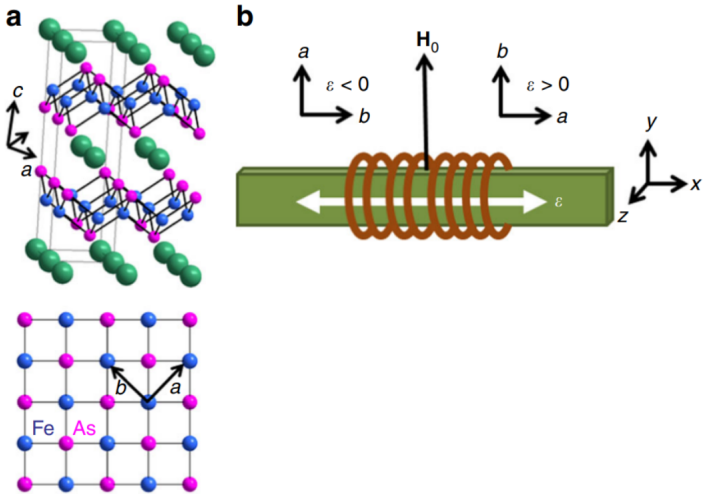

FIGURE 3.1: (a) Crystal structure of BaFe2As2, with Ba (green), Fe (blue) and As (magenta) sites shown. Lower panel shows the Fe-As plane in the tetragonal phase, with arrows indicating the unit cell axes of the orthorhombic phase (a||(110)tet, b||(110)tet). (b) Orientation of the magnetic field with respect to the coil H_1 and strain axis for $H_0 \perp c$.

As mentioned earlier, the ^{75}As quadrupolar moment couples closely with the EFG. We define V_{aa} and V_{bb} as components of the EFG in the [100] (a) and [010] (b) crystal directions in the orthorhombic phase (Fig 3.1). The addition of stain fields will break the tetragonal symmetry of the EFG, similar to the zero strain EFG behavior at the natural phase transition. Our specific crystal was synthesized through a self flux method, and cut along the Fe-Fe bonds (the (110) direction in tetragonal phase) to approximately 1.5cm x 0.5cm (Cite my paper here). The following section outlines the setup of the sample and other hardware.

3.2 Setup

The apparatus needed to provide controlled tensile and compressive stress to $BaFe_2As_2$ in order to create the pulsed strain fields. We elected to use the RazorbillTM CS100 piezoelectric strain device (3.2), which applies a voltage difference across the piezoelectric stacks, resulting in a contraction or stretching of the sample. We determine the actual displacement of the sample by measuring the capacitance of the system and calibrate the strain as a function of applied voltage.

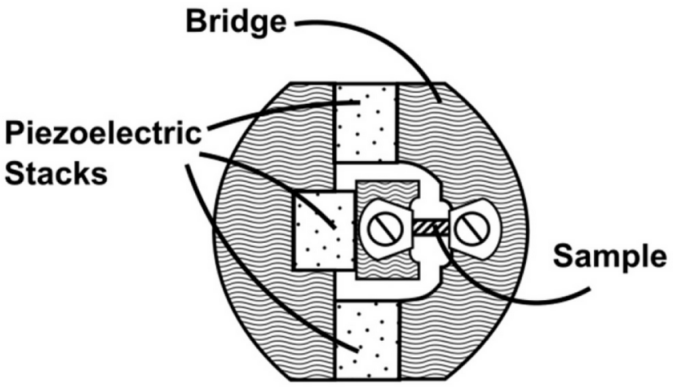

FIGURE 3.2: Geometry of the piezoelectric device.

The piezo stacks have three connections total. We utilize two of the connections to apply a pulsed strain sequence on top of a baseline static strain, which was applied using the third connection. The constant strain ensures that there is no drifting

from the baseline displacement as an experiment evolves. The displacement is monitored using proportional integral derivative (PID) control. The CS100 chassis is made of titanium, which has a very low magnetic susceptibility and should not affect the homogeneity of a magnetic field at the sample site. Two mounting pieces sit along the strain axis at a distance chosen to accommodate the NMR coil. Epoxy was used to secure the crystal at all steps of the process. Fig 3.3 shows the crystal, wrapped in coils of wire to apply RF pulses and detect response currents, on the device head.

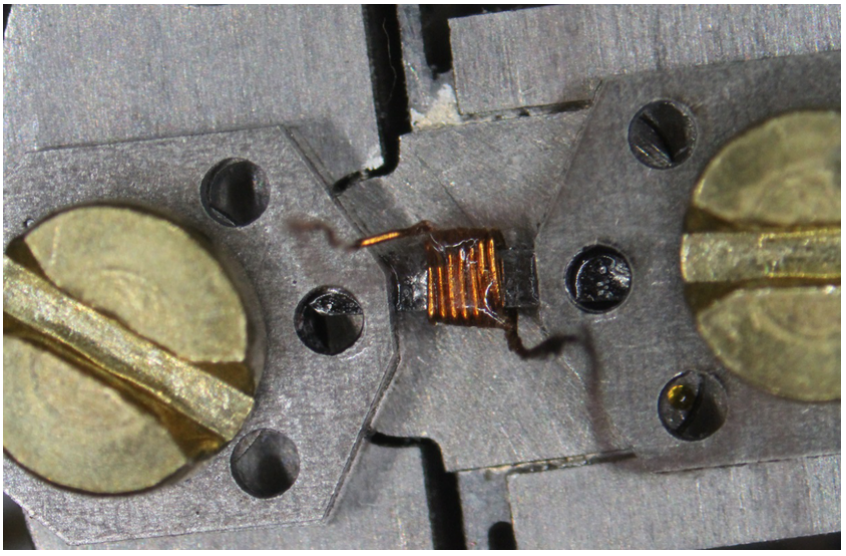

FIGURE 3.3: Sample attatched to RazorbillTM CS100.

The RazorbillTM CS100 is just one part of a much larger probe head that moderates voltage application, capacitor tuning, and RF applications for the piezoelectric device. High power RF pulses reach the sample using semi-rigid coaxial cables and two cryogenic capacitors Kissikov et al. (2017a). Impedance matching is important to ensure the capacitance bridge and other electronics work properly. Fig 3.4 is a schematic for the probe head, which is attached to a nearly 2m probe to place the crystal at the correct position in our magnetic field.

A static external magnetic field is generated by our Oxford electro-magnet. Employing a superconducting coil that carries 120 A, the magnet generates a magnetic field of around 11.7 T. At the site of the sample, this field is extremely uniform and

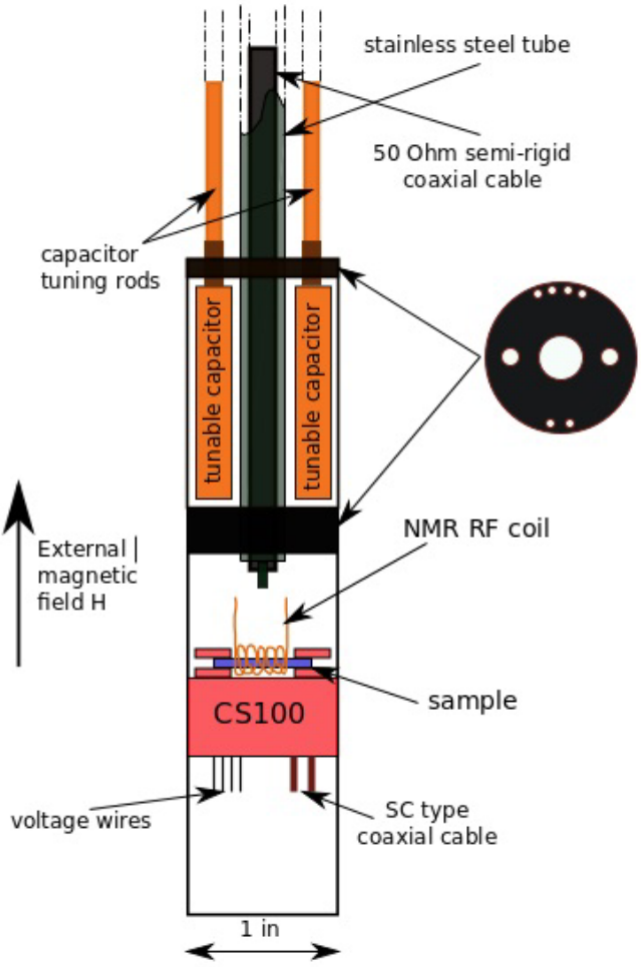

FIGURE 3.4: Schematic diagram of the probe head, including two not previously mentioned flexible coaxial cables for the capacitive displacement meter.

is thus suitable for high-precision NMR measurements. A cryostat is used to keep the magnet cold, the outer layer of liquid nitrogen is around 77k and the liquid helium surrounding the NMR coils is approximately 4k. The temperature at the sample location is independently controlled and the coils are used to excite the sample using RF pulses. The next section outlines the electronics needed supply the voltage pulses, which are applied to the piezoelectric device in order to create strain.

3.3 Pulse Generation

We needed a setup that could apply precise strain pulses relative to the Hahn Echo RF pulse sequence. To do so, we employed TTL pulses from an NMR spectrometer to drive analog switches and were timed to immediately follow the $\frac{\pi}{2}$ and π RF pulses. Once the switch is on, a strain pulse of amplitude V_p is applied for a time t_p, at which point the pulse amplitude is flipped to -V_p. This pulse is also applied for a time t_p, and is afterwards turned off. The voltage across the piezo stack does not reach $\pm V_p$ immediately, and thus the strain is not a perfect square wave. The phase of a resulting echo signal will be proportional to $V_p \times t_p$. A resistance R = 100Ω shown in the circuit diagram (Fig 3.5) is in parallel with the piezo stack, which has an intrinsic capacitance ($\sim 2\mu F$) and the RC values were chosen to create a rise time (for the voltage) shorter than T_2. This way strain can be applied comfortably between RF pulses.

The time between RF excitation pulses, τ, governed how long we could apply strain. Our pulses were not perfectly square. Lengthening τ was a way to minimize the effects of the voltage rise time and keep the average voltage magnitude as close to V_p as possible. However, if τ was too long, we experienced a loss of signal do to the T_2 decoherence effects described in Chapter 1. We strike a balance of these two factors by considering the T_2 decay constant, at which point the signal is $\frac{1}{e}$ that of the original. T_2 was measured to be approximately 700 μs in $BaFe_2As_2$, so we landed on setting τ (and thus t_p) to be 670 μs. Fig 3.6 shows the original pulses at 200 μs to a longer 670 μs pulse length used in the actual experiment.

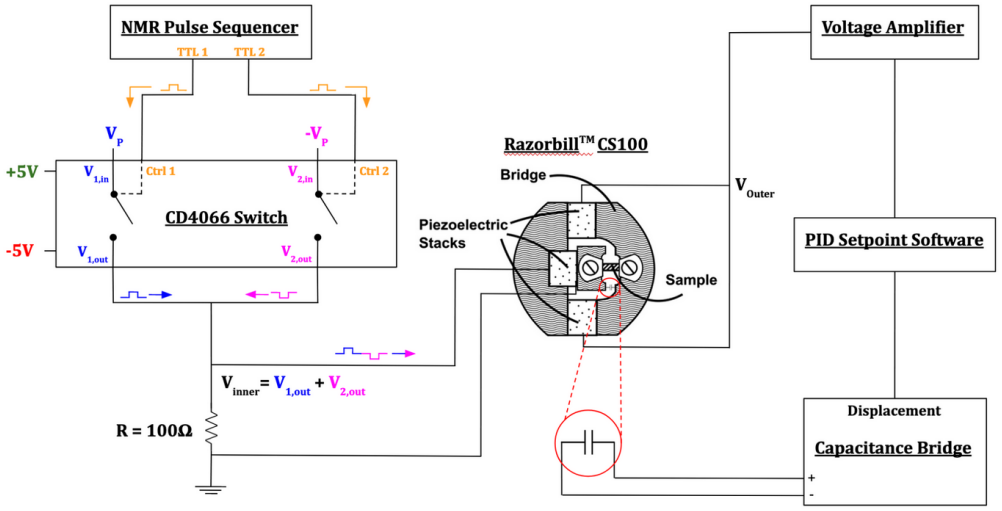

FIGURE 3.5: Circuit diagram illustrating the creation of voltage pulses. TTL pulses control an analog switch using DC voltages set to $\pm V_p$, which manage the inner stack of the CS100 device. The outer stack is held at a constant displacement using PID feedback control. Cite Cameron here!

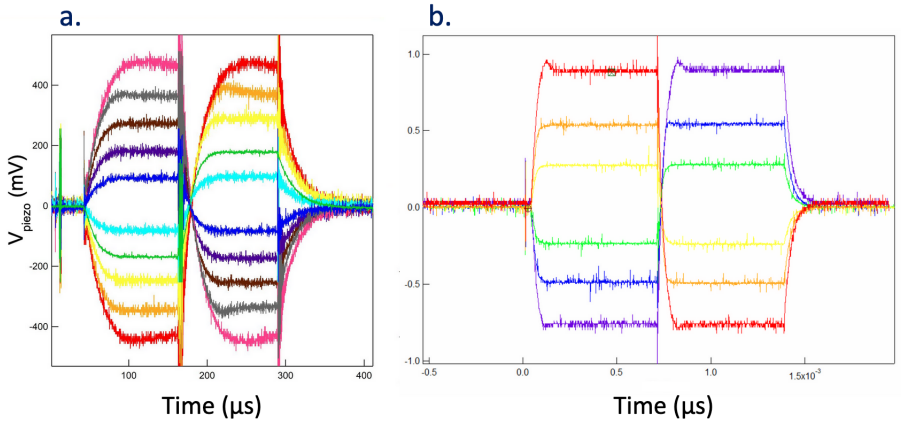

FIGURE 3.6: (a) Measured voltage across the inner stack as a function of time for ten different values of V_p and a pulse length of $200\mu s$. (b) Measured voltage across the inner stack as a function of time for six different values of V_p and a pulse length of $670\mu s$.

3.4 Procedure

At each targeted temperature, a frequency sweep was conducted to identify the resonance frequency of a given transition for the nucleus under unstrained conditions. The sweep was designed to test a series of frequencies that centered around previously published values for the resonance, and the resulting echo magnitudes were fit to a Gaussian curve in order to find the experimental center. We adjust the radiofrequency output of the NMR software to reflect the new frequency.

With the unstrained case characterized, we moved on to implement a voltage sweep, which in turn caused strain pulses, in the fashion discussed in Section 3.3. Sweeps ranged from -2V to 2V, values small enough as to not introduce any oscillations in the piezo device due to natural vibrational resonances. Our experiment utilized signal averaging to improve the signal to noise ratio. Each measurement lasted on the order of 10 μs, so an experiment consisting of ten million sequences requires on the order of 10 hours to perform. A baseline correction of the averaged signal reveals a clear echo at time 2τ. Quadrature detection gives the S_x and S_y projections of the echo pulse, often referred to as 'real' and 'imaginary' signals respectively. S_x and S_y signals will be out of phase with zero strain case by an amount proportional to the magnitude and length of the applied strain. The Fourier transform of the S_x and S_y contributions to the echo were exported to analysis software where we can characterize the experiment further. We estimate the strain from applied voltage using a temperature dependent calibration factor ϵ/V_p, which is determined by measurements of the displacement under constant voltage.

CHAPTER 4: Results and Analysis

4.1 Static Strain Results

In this section, we review the results from a previous static strain experiment, where a constant strain was applied to $BaFe_2As_2$ and the shifts in ^{75}As resonance frequencies were measured directly. We present the findings here, and will use them as reference for our survey of pulsed strain.

The central transition of ^{75}As does not move under strain, so we express a shift in a satellite resonance frequency as a change in the quadrupolar splitting of the nucleus. Here, the quadrupolar coupling is just the difference between the central and satellite transition frequencies of ^{75}As. Fig 4.1 shows the measured quadrupolar splitting of $BaFe_2As_2$ in each direction as a function of temperature, with the magnitude of static strain as an implicit parameter (color). It also includes the zero strain quadrupolar splittings of $BaFe_2As_2$ in black.

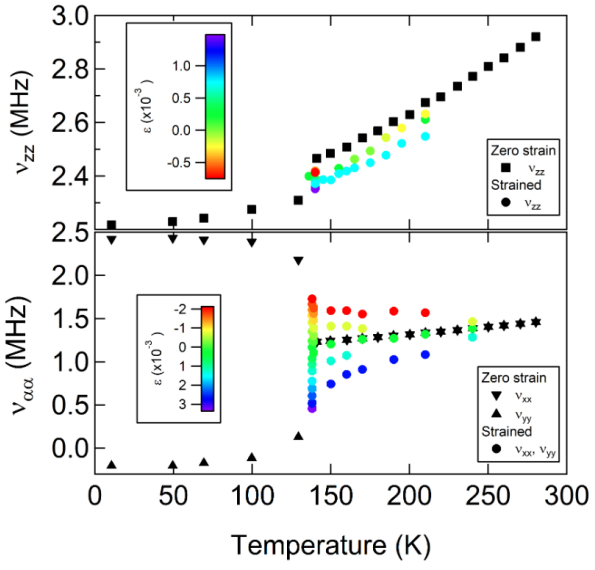

FIGURE 4.1: Components of the As EFG $(\nu_{xx}, \nu_{yy}, \nu_{zz})$ vs temperature for $BaFe_2As_2$ under zero and then uniaxial strain.

The vertical axis shows the splitting in MHz, while the horizontal axis is the the crystal temperature. Fig 4.1 suggests that applied strain significantly alters the local EFG. In this case, the strained EFG values approach those of an unstrained crystal below the natural phase transition. Notice that it isn't until the introduction of nematic order (by the natural phase transition or applied strain) that $\nu_{xx} \neq \nu_{yy}$. This makes it easy to identify a zero-strain displacement. With the sample oriented so that H_0 is perpendicular to the c crystalline axis (Fig 3.1), $\nu_{yy} = \nu_{aa}$ for compressive strain ($\epsilon < 0$) and $\nu_{yy} = \nu_{bb}$ for tensile strain ($\epsilon > 0$). Additionally, $\nu_{xx}(\epsilon) = \nu_{yy}(-\epsilon)$. Technically the stress will also induce strains that correspond to other elastic modes, but the effect is dominated by the in-plane uniaxial strain (Kissikov et al. (2017b)).

Fig 4.2 takes a closer look at the ν_{yy} splitting as a function of strain at a series of different temperatures. It is clear that the EFG response is linearly proportional to in-plane strain, with the slope dependent on temperature, confirming that shifts in satellite frequencies can be used to measure the local nematicity of the crystal.

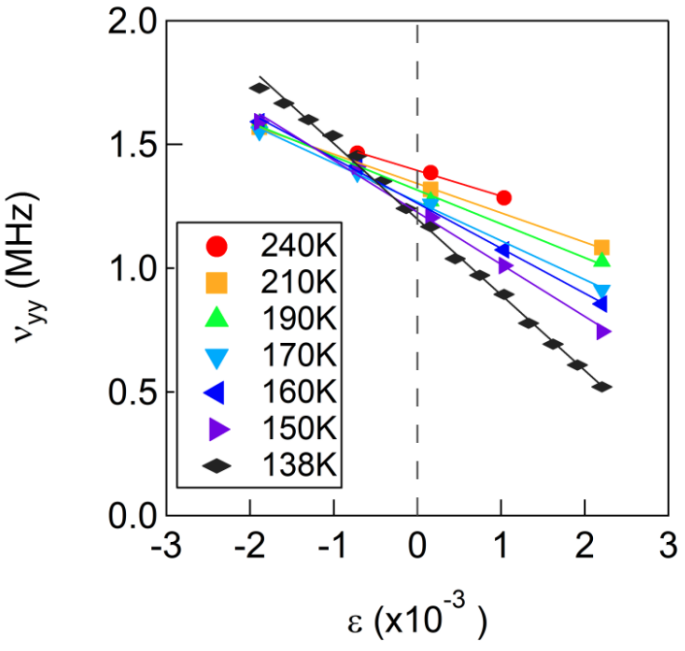

FIGURE 4.2: The quadrupolar splitting ν_{yy} as a function of strain for multiple fixed temperatures.

We are interested in how the nematic susceptibility behaves as a function of temperature, which has previously been explored through Elastoresistance and other experimental methods. These techniques fit the nematic susceptibility measurements to a Curie-Weiss curve, the model for how magnetic susceptibility diverges near a phase transition, because the nematic susceptibility also diverges as the temperature approaches the structural transition (135K). The accuracy of the static strain technique can be confirmed by comparing the measurements to previous results. After extracting the slopes from Fig 4.2 as a function of temperature, they are compared with elastoresistance measurements in Fig 4.3. The NMR data values are presented as the change in η as a function of strain, ϵ.

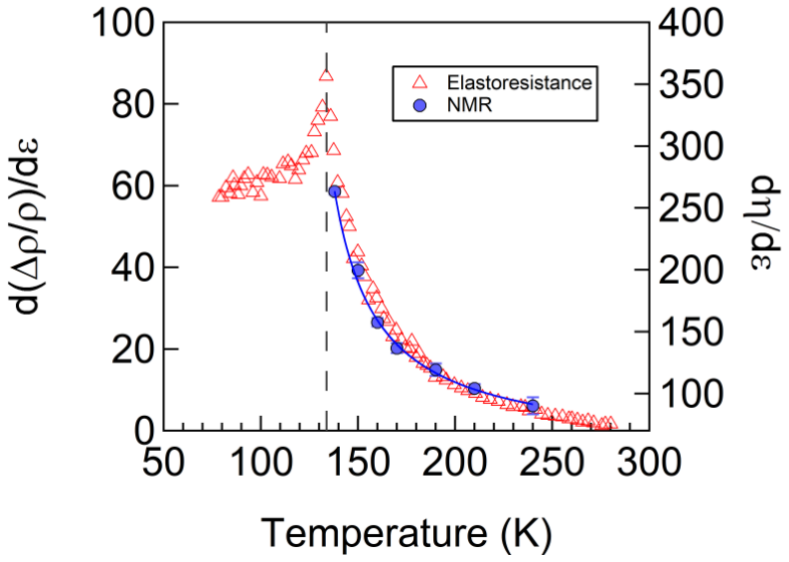

FIGURE 4.3: The nematic susceptibility measured through EFG asymmetry vs elastoresistance (reproduced from Jiun - Haw) measurements.

The static strain technique agrees closely with Elastoresistance values, observing the same divergence near the phase transition. As a result, we are confident that the NMR method correctly measures the nematic susceptibility of $BaFe_2As_2$. The next section investigates the results of our pulsed strain technique, and compares the data to static measurements.

4.2 Pulsed Strain Results

We will now show how pulsed strain can measure the same nematic susceptibility using significantly smaller magnitudes of strain. A method requiring less strain is at a clear advantage when working with more fragile materials. As mentioned earlier, pulsed strain will change the phase acquired by nuclear spins during precession, rather than shifting a resonance frequency directly. This phase rotation can be seen through the relative intensities of the spin x (S_x) and spin y (S_y) spectra, and is proportional to the magnitude and length of the applied strain pulse. One can obtain the phase angle through $\theta = arctan(I_y/I_x)$, where θ is cycles and $I_{x,y}$ are the integrated intensities of the S_x and S_y spectra.

We measure this phase change as a function of strain for each transition, and then repeat the process at a series of temperatures. The top row of Fig 4.4 begins by showing the normalized spectra for S_x and S_y as a function of voltage for each of the ^{75}As transitions. The top left graph shows the S_x and S_y spectra for the upper satellite transition at five different applied voltages. The upper middle graph shows the spectra for the central transition at nine different applied voltages. The top right graph then shows the spectra for the lower satellite transition at five different applied voltages. The bottom row of graphs is an alternative way to depict the phase relationship between the S_x and S_y, and corresponds to the same transition probed by the spectrum above it. In these graphs, the intensity of S_x and S_y are plotted with frequency as an implicit parameter.

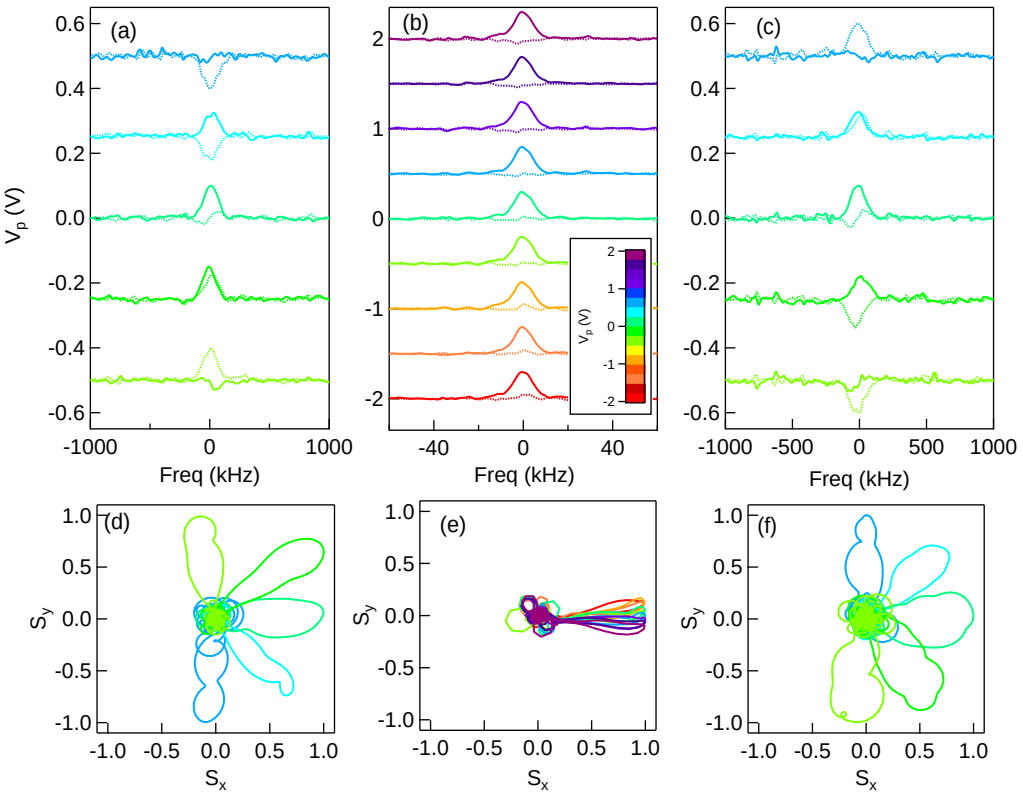

FIGURE 4.4: Normalized spectra vs frequency for the (a) upper, (b) central and (c) lower transitions of ^{75}As. Solid and dotted lines correspond to the projection along the x and y axes in the rotating frame. Each frequency axis is offset by the corresponding resonance frequency of that transition, and the vertical axes have been offset by the value of V_p. Graphs (d), (e) and (f) show the same data, but explicitly plot S_x verses S_y with frequency as an implicit parameter. The color scale portrays V_p and remains the same across all plots.

It is clear that for each of the satellite transitions, the relative intensities of the S_x and S_y spectra are heavily dependent on strain. Meanwhile, the central transition is unaffected by strain all together, just as in the static strain experiment. The phase relationship is even more evident in the bottom row of plots. Here, a single graph 'peaks' at a different ratio of S_x to S_y for each applied voltage, showing the progression of phase as strain is increased or decreased. These plots should be compared to Fig 2.5 in Chapter 2, where theoretical simulations observed the same phase accumulation.

For each value of strain, the phase difference between S_x and S_y can be converted into a frequency shift through $\Delta f = \frac{\theta}{2t_p}$. Fig 4.5 plots the calculated frequency

shift as a function of pulsed strain magnitude for the upper satellite (blue), lower satellite (red) and central (black) transitions. The vertical axis has units of Hz and the horizontal axis is given as strain $\times 10^6$.

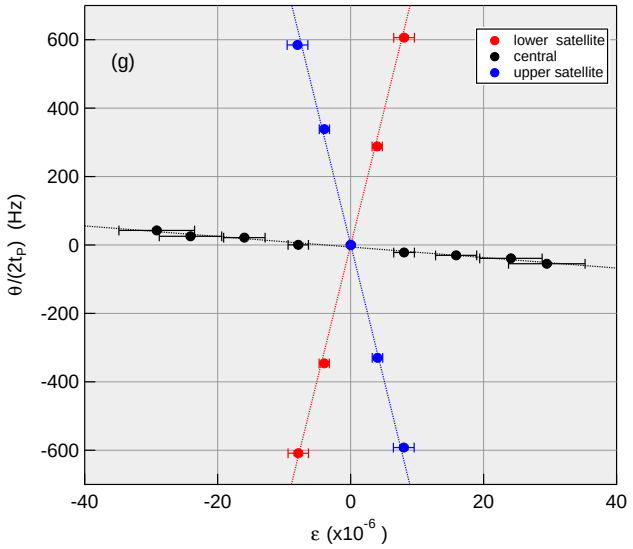

FIGURE 4.5: Echo phase over strain pulse time (in cycles per second) versus applied strain at 140K. The dotted lines indicate linear fits with slopes $\partial f_-/\partial\varepsilon = 78 \pm 8$ MHz/strain, $\partial f_0/\partial\varepsilon = -1.5 \pm 0.1$ MHz/strain, and $\partial f_+/\partial\varepsilon = -79 \pm 8$ MHz/strain.

We find that the resonance frequencies have a linear response to an applied strain pulse, our first indicator that we are indeed measuring the nematic susceptibility of the crystal. The slopes of the echo response match the QuTIP numerical simulations discussed in Chapter 2, which used realistic pulse widths and modelled the strain as a time depended η. The close agreement is very important, and is a justification for the use of perturbation theory to express transition frequencies in atomic nuclei.

We repeated the measurement at multiple temperatures to measure the change in nematic susceptibility as we approach the phase transition. Fig 4.6 (a) displays the lower transition response for a series of different temperatures, with the calculated frequency shift in units of Hz and the horizontal axis in units of strain $\times 10^{-6}$.

(b) plots the slope of each response as a function of temperature. The inset of (b) plots the inverse of nematic susceptibility with respect to temperature. For these experiments, the crystal displacement was held constant as the temperature was lowered. As a result, there is a positive residual strain due to the thermal contraction of the sample. We estimated this residual strain by measuring the EFG splitting of the satellite frequencies under zero strain. Both graphs in (b) contain fits with (solid) and without (dashed) residual strain.

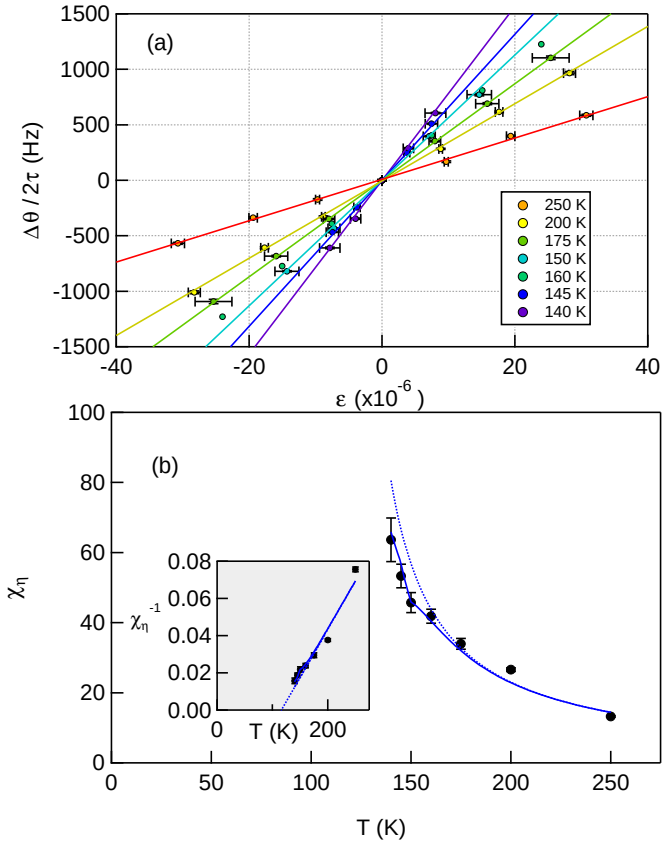

FIGURE 4.6: (a) Frequency shift of lower satellite as a function of strain for several temperatures. Solid lines show linear fits of the data. (b) Nematic susceptibility, χ_η, as a function of temperature. The solid and dashed lines are fits with and without residual strain. The inset explores how the inverse of susceptibility changes with temperature.

The pulsed strain causes a linear response at all temperatures, and the nematic susceptibility diverges as we approach the phase transition at 135K. To confirm the accuracy of the data, we would like to compare the slopes to those of the

static strain measurements. Fig 4.7 plots the NMR frequency shifts measured by static and pulsed strain. The vertical axis is a log scale of the measured frequencies and the horizontal axis indicates the log of the magnitude of applied strain. The temperature at which the static (⧫) and pulsed (•) strains were applied is given by the color. The green and red horizontal lines indicate the homogeneous (T_2^{-1}) and inhomogeneous (T_{2*}^{-1}) line widths in this material, which limit the sensitivity of measuring a frequency shift using static strain. On the other hand, the minimum detectable frequency using pulsed strain is determined by the precision of the phase angle of the echo signal. Our instruments had a precision of $\approx 0.5\,\text{deg}$ for a spectrum with a signal to noise ratio of 5×10^6. Using the measured $T_2 = 692\mu s$, this corresponds to a minimum detectable shift of $1Hz$, shown as the blue horizontal line. The lowest frequency shift we measured in the lab setting was $\approx 76Hz$.

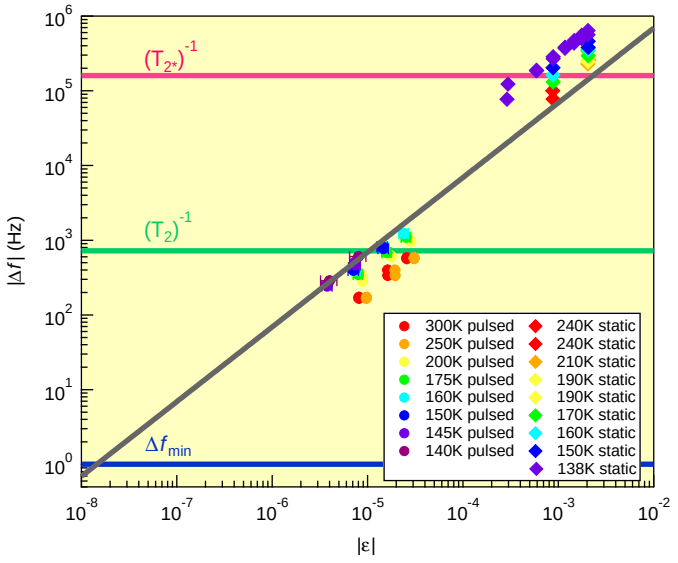

FIGURE 4.7: Comparison of the frequency offset, $|\Delta f|$, versus strain, ε, measured by static (⧫, reproduced from (cite kissikov) and pulsed (•) techniques. The pink and green lines correspond to T_{2*}^{-1} and T_2^{-1} for $BaFe_2As_2$, respectively, and the blue line corresponds to the minimum detection level, as discussed in the text.

Fig 4.7 shows that the pulsed strain technique manages to measure slopes that are approximately equal to those measured in the static case for each of the temperatures, despite several orders of magnitude difference in the strain. This result supports the use of pulsed strain and NMR to measure nematic susceptibility in a

wider range of materials than were previously accessible. The new technique also avoids the problems associated with extremely short (T_{2*}^{-1}) times for iron-based superconductors in their critical regime.

CHAPTER 5: Conclusion

Pulsed strain can expand the use of NMR-based measurements of nematic susceptibility to a much larger range of materials. Compounds with inhomogeneous line widths, such as iron-based superconductors, had previously been a barrier to the static techniques and should be much more accessible with our new method. Measurements of nematic susceptibility have previously been done on these materials in the disordered phase, but only pulsed-strain has the capability of probing these characteristics below critical temperatures in superconductors. The signal from a single crystal is usually reduced in the critical regime due to smaller penetration depths, a problem that can be solved by the increased sensitivity of our method. An increase in sensitivity also provides the opportunity to examine more fragile materials that would not be able to stand large strain values.

In the future, we look to investigate $CaKFe_4As_4$, which seems particularly promising for the new technique. $CaKFe_4As_4$ is superconductive and a slightly altered version of Ba_4As_4 that has the potential to behave similarly when subjected to strain. Elastoresistance measurements indicate an enhanced nematic susceptibility in the normal phase despite the material having a high critical temperature. Our technique looks to observe changes in the susceptibility within the critical state in an effort to deduce the contributions of nematic fluctuations in stabilizing superconductivity. At the very least, understanding the EFG response can lend insight into electric structure in strongly correlated materials.

Bibliography

Curro, N. J., Kissikov, T., Tanatar, M. A., et al. 2022, Front. Phys., 10, doi:10.3389/fphy.2022.877628

Johansson, J., Nation, P., & Nori, F. 2012, Comput. Phys. Commun., 183, 1760

Kissikov, T., Sarkar, R., Lawson, M., et al. 2017a, Review of Scientific Instruments, 88, doi:10.1063/1.5002631

—. 2017b, Phys. Rev. B, 96, 241108(R)

—. 2018, Nat. Commun., 9, 1058

Kitagawa, K., Katayama, N., Ohgushi, K., Yoshida, M., & Takigawa, M. 2008, J. Phys. Soc. Jpn., 77, 114709